Tuning Both Anionic and Cationic Redox Chemistry of Li-rich $Li_{1.2}Mn_{0.6}Ni_{0.2}O_2$ via a "Three-in-One" Strategy

Qingyuan Li[1], De Ning[2,3], Dong Zhou[2], Ke An[4], Götz Schuck[2], Deniz Wong[2], Weijin Kong[1], Christian Schulz[2], Gerhard Schumacher[2] and Xiangfeng Liu[1,5]*

[1]Center of Materials Science and Optoelectronics Engineering, College of Materials Science and Optoelectronic Technology, University of Chinese Academy of Sciences, Beijing 100049, P. R. China

[2]Helmholtz-Center Berlin for Materials and Energy, Hahn-Meitner-Platz 1, Berlin 14109, Germany

[3]Center for Photonics Information and Energy Materials, Shenzhen Institutes of Advanced Technology, Chinese Academy of Sciences, Shenzhen 518055, P.R. China

[4]Neutron Scattering Division, Oak Ridge National Laboratory, Oak Ridge, Tennessee, 37830, USA

[5]CAS Center for Excellence in Topological Quantum Computation, University of Chinese Academy of Sciences, Beijing 100190, China

*E-mail: liuxf@ucas.ac.cn

Abstract

Anionic redox chemistry endows Li-rich layered oxides cathode with the high specific capacity but it also causes some critical issues such as the voltage decay, structure degradation and irreversible oxygen release. Herein, we propose to tune both the anionic and cationic redox chemistry of $Li_{1.2}Mn_{0.6}Ni_{0.2}O_2$ via a "Three-in-One" strategy integrating Na doping for Li site, Si substitution for Mn and Na_2SiO_3 coating layer, which is achieved by the facile coating of Na^+-conductive Na_2SiO_3. In comparison with pristine or Li_2SiO_3-coating sample, the concerns of voltage fading, poor rate capability, structure degradation and oxygen release have all been largely alleviated due to "Three-in-One" effect. Firstly, the coating layer impedes the side reaction and the dissolution of transition metal (TM). Secondly, the Na^+ is confirmed to be doped into the Li layers to facilitate the transport kinetics of lithium ion while Si^{4+} is doped into the transition metal site, which enhances the stability of the layered structure during cycling due to the strong Si-O bond and reduces the migration of TM. Thirdly, the integrated strategy also decreases the covalency of TM-O bonds, which is verified to improve the reversibility of anion redox chemistry and suppress oxygen evolution. The synergetic strategy sheds some lights on exploring high-performance cathode materials by tuning both anionic and cationic redox chemistry.

1. Introduction

Lithium ion batteries (LIBs) have been widely applied in portable electronic devices, smart grid and electric transportations.[1-7] Cathode materials as a key component of LIBs play a crucial role on the overall performance of the batteries, and the cathode materials with a high energy density, long lifetime and high safety are urgently needed to meet the requirement of electric vehicles.

Due to the high specific capacity (~300 mAh g^{-1}), which origins from the anionic and cationic redox chemistry, Li-rich Mn (LRM) based layered oxide materials are considered to be the most promising candidate for the next generation LIBs. However, these cathode materials still suffer from significant shortcomings such as voltage fading, capacity decay, poor rate capability and O_2 irreversible release. To overcome these problems and to maintain the activity of oxygen and transition metals (TMs) redox chemistry, some strategies including but not limited to doping and surface coating are reported. Guo et al. and Abraham et al. reported that Na^+ substitution into the Li^+ slab of the layered structure could enhance the kinetics of Li^+ migration.[8, 9] Meng et al. also reported the cationic doping in Li-rich cathode could mitigate the oxygen release and maintained the activity of anionic redox reaction.[10] Xia et al. have suggested that the reversibility of anion redox chemistry can be enhanced by Si doping to tune the electronic structure of Li-rich cathodes.[11] Recently, the synergy of surface and bulk doping or cation and anion co-substitution to improve the electrochemical performances of cathode materials has also been explored.[12-16] It has been verified that surface coating by spinel $Li_4Mn_5O_{12}$ can suppress the loss of lattice oxygen and enhance

3

the anionic redox chemistry.[17] Moreover, we also reported Li_2SnO_3 coating was conducive to the comprehensive electrochemical performances due to the enhancement of activity and reversibility of anion redox chemistry.[18] In order to tune the anionic redox chemistry, these pioneering studies open a bright door for adjustment of the crystal or surface structure of cathode materials. However, it is still highly desirable to explore effective strategies to further improve the anionic redox chemistry and unravel the underlying relationship between crystal or electronic structure change and the enhanced electrochemical performances.

Herein, we propose to simultaneously improve the anionic and cationic redox chemistry of cobalt-free $Li_{1.2}Mn_{0.6}Ni_{0.2}O_2$ via an integrated "Three-in-One" strategy combining the advantages of Li doping for Na site, Si substitution for Mn and Na_2SiO_3 coating layer, which has been achieved by the facile coating of Na^+-conductive Na_2SiO_3. In comparison with the pristine or Li_2SiO_3-coating sample, the key problems, such as the voltage fading, poor rate capability, structure degradation and oxygen release, have all been largely alleviated. The synergic mechanism has been unraveled by means of neutron powder diffraction (NPD), *in situ* X-ray diffraction (XRD), spherical aberration correction scanning transmission electron microscope (sAC-STEM), *ex situ* X-ray absorption spectra (XAS) and resonant inelastic X-ray scattering (RIXS), operando differential electrochemical mass spectrometry (DEMS) and density functional theory (DFT) calculations.

2. Experimental Section

Synthesis: The pristine Li-rich Mn based material, $Li_{1.2}Mn_{0.6}Ni_{0.2}O_2$ (LMNO), can be

synthesized by the procedure in our previous report.[18] The modified sample Na_2SiO_3@LMNO (NSO) is prepared according to the process. A certain quality pristine LMNO is dispersed into deionized water and ammonia water, then, this mixture is ultrasonic for five minutes. After that, a stoichiometric amount of tetraethyl orthosilicate (TEOS) is added into the solution, the Si content is calculated following the mass ratio of Na_2SiO_3/LMNO = 1%. This solution is stirred for 12h at 700 r/min, followed by centrifuging and washing with deionized water and ethanol. At last, the as centrifuged material is mixed with a stoichiometric amount of Na_2CO_3 and calcined at 750 ℃ for 12h.

Characterization: The crystal structure is characterized by XRD (Rigaku, Smartlab, 9 kW) in the scan range of $10^o – 80^o$ with $1^o\,min^{-1}$. High-resolution transmission electron microscopy (HRTEM, F20) is carried out to characterize the coating. The elemental distribution mapping is characterized by an energy-dispersive X-ray (EDX) spectroscopy attached to a field emission scanning electron microscopy (FESEM, Hitachi-SU8010). Images of atomic arrangement are acquired using an aberration corrected scanning transmission electron microscope (JEM, ARM200F). The *in situ* XRD is carried out in the 2theta range of $10^o – 46^o$ on the SMARTLAB with a scan rate of $15^o\,min^{-1}$. XPS is measured with an Al Kα achromatic X-ray source on the ESCALAB 250Xi (Thermo Scientific). Differential scanning calorimeter (DSC, Q2000) is applied to confirm the thermal stability of materials. XAS is measured at beamline KMC2 of Bessy II synchrotron radiation facility with the transmission mode at Helmholtz-Zentrum Berlin für Materialien und Energie (HZB, Berlin, Germany), and

the RIXS are characterized at beamline U41-PEAXIS of Bessy II, HZB, Berlin, Germany.

Electrochemical experiments: The positive electrodes are prepared using the active material, carbon black and polyvinylidene fluoride (PVDF) according to the mass ratio of 80:10:10 in the appropriate amount of N-methyl pyrrolidinone (NMP). This slurry is loaded on aluminum foil current collector and dried at 80 ºC until the liquid disappears, then it is transferred to the vacuum drying oven for 12 h at 120 ºC. At last the 2025-type coin cells are prepared in an argon-filled glove box. The electrochemical performances are measured by galvanostatic charge-discharge process using battery testers (NEWARE) between 2.0 – 4.8 V. The electrochemical impedance spectroscopy (EIS) and the potentiostatic intermittent titration technique (PITT) are conducted by the electrochemical workstation (Metrohm-Autolab, PGSTAT 302N). Operando differential electrochemical mass spectrometry (DEMS, Linglu) was performed to measure the oxygen release.

Neutron powder diffraction (NPD): The data are measured at the VULCAN beamline of the Spallation Neutron Source (SNS) in the Oak Ridge National Laboratory.[19, 20] The size of the incident beam is 5×12 mm, and it is 5 mm for the receiving collimator. A double-disk chopper at a speed of 30 Hz is used to select an incident beam with a bandwidth of 0.7-3.5 Å. There is a d-space of 0.5-2.5 Å in the diffraction pattern in the $\theta \pm 90º$ detector banks. The value of $\Delta d/d$ is approximately 0.25% at the high-resolution mode. The power of the SNS is nominally 1400 kW, the data is collected at room temperature for 3 h, and the VDRIVE software is used to reduce the data. The SNS data

are preprocessed by the EXPGUI-GSAS program.[21] The joint refinement against both

XRD and NPD data is conducted by TOPAS program.

Computation method: First-principle calculations were performed by the density

functional theory (DFT) using the Vienna Ab-initio Simulation Package (VASP)

package.[22] The generalized gradient approximation (GGA) with the Perdew-Burke-

Ernzerhof (PBE) functional were used to describe the electronic exchange and

correlation effects.[23-25] Uniform G-centered k-points meshes with a resolution of

$2\pi \times 0.03$ Å^{-1} and Methfessel-Paxton electronic smearing were adopted for the

integration in the Brillouin zone for geometric optimization. The simulation was run

with a cutoff energy of 500 eV throughout the computations. These settings ensure

convergence of the total energies to within 1 meV per atom. Structure relaxation

proceeded until all forces on atoms were less than 1 meV Å^{-1} and the total stress tensor

was within 0.01 GPa of the target value.

In this system, the $Li_3Mn_3O_6$ (space group: $R\bar{3}m$) was chosen as the initial

structure. We then built a 5*1*1 supercell of $Li_3Mn_3O_6$ to get the $Li_{15}Mn_{15}O_{30}$ structure.

For $Li_{1.2}Mn_{0.6}Ni_{0.2}O_2$ composition, we randomly replaced three Mn atoms with Li, and

three Mn atoms with Ni to get $Li_{18}Mn_9Ni_3O_{30}$. For the coated $Li_{1.2}Mn_{0.6}Ni_{0.2}O_2$ sample

by NSO, our experimental results show that Na^+ enters the Li ion layer in the bulk phase,

and Si^{4+} enters the transition metal layer. So, we replace one of the Li atoms (Li ion

layers) by one Na atom and one of the Mn atoms (transition metal layers) by one Si

atom. Due to the strong-correlation of d electrons in Mn and Ni, a U−J parameter of

5.25 eV and 5.77 eV were applied. The energy barrier for the diffusion of Li atom was

calculated using the nudged elastic band (NEB) method. The calculation parameters and convergence criteria were kept the same as in the ground state calculations.

3. Results and discussion

The crystal structures of the pristine $Li_{1.2}Mn_{0.6}Ni_{0.2}O_2$ (LMNO) and Na_2SiO_3 coated samples (NSO) are characterized by NPD and powder XRD as shown in Figure 1 and Figure S1. The joint refinement is conducted using NPD and XRD because of the sensitivity of NPD to light elements, [26] and the refinement patterns of both samples are only indexed to layered α-NaFeO$_2$ structure with the R$\overline{3}$m space group due to the small proportion of monoclinic phase. And the joint refinement results of both samples are shown in Table 1 and the detailed site occupation is shown in Table S1. The R_{wp} values of pristine and NSO are 3.92% and 3.34%, respectively, which indicates the curves are well fitted. We can clearly find the lattice parameters a and c are increased, which means Na and Si have been successfully doped into the bulk phase. This also can be verified by moving the peak (003) to a small angle (Figure S1a). However, the radius of Si^{4+} is smaller (0.4 Å) than that of manganese and nickel ions, but the Na^+ is larger (1.02 Å) than that of Li^+, which means the doping effect of Na^+ for lattice structure is more obvious than that of Si^{4+}. To further investigate the stability of structure and kinetics of Li ion diffusion, the slab thickness $S_{(MO2)}$ and interslab spacing $I_{(LiO2)}$ of both samples are calculated by the formula: $S_{(MO2)}=2[1/3-Z_{ox}]c$ and $I_{(LiO2)}=c/3- S_{(MO2)}$.[27, 28] The increase in the inter slab ($I_{(LiO2)}$) illustrates Na^+ has doped into the Li^+ layer, which can be used to improve the Li^+ diffusion as a pillar due to the larger radius of Na^+ compared with that of Li^+. As a comparison, the thickness of the TM layer of NSO is smaller

8

indicating the small radius Si^{4+} substituted the TM layer. This decreased slab thickness is favorable to the stability of the structure. As shown in Table 1, the TM-O bonds length of NSO are increased compared to the pristine material, which means the slight reduction of TM-O covalency of NSO, and this can decrease the oxygen release to enhance the stability of structure.[29, 30] The above analysis proves the elements Na^+ and Si^{4+} of coating layer have successfully doped into the surface of LMNO cathode material which stabilizes the crystal structure.

Table 1. The joint refined results for both samples

Sample	a (Å)	c (Å)	V (Å^3)	Z_{ox}	$S_{(MO2)}$ (Å)	$I_{(LiO2)}$ (Å)	TM-O (Å)	R_{wp} (%)
Pristine	2.8589(1)	14.2535(4)	100.911(3)	0.2420(1)	2.6034	2.1478	1.9603(2)	3.92
NSO	2.8592(1)	14.2536(4)	100.892(4)	0.2425(1)	2.5891	2.1621	1.9662(2)	3.34

To confirm the Na_2SiO_3 coating layer has been coated successfully on the surface of the pristine material, the TEM is used to characterize the morphology. Figure S2a shows the image of the pristine sample, and the green line shows the boundary between the surface of the sample and the carbon support film on the copper mesh, and no coating was found. As a comparison, Figure S2b shows the high resolution TEM image of the NSO sample. We can clearly see the different lattice fringe in the bulk and coating layer. The lattice spacing are 0.47 nm and 0.30 nm, respectively, which are in line with the (003) plane of LRM and the (110) plane of Na_2SiO_3. Moreover, to observe the distribution of elements more intuitively, the EDX mapping images of NSO sample are presented in the Figure S2c-h, which can illustrate the uniformity of coating. Based on the results of X-ray diffraction, the HRTEM and SEM, the coating has been verified.

To further observe the doping effect intuitively, sAC-STEM has been applied. Figure 1c-e shows atomic-revolution images and corresponding converting patterns, where the transition metal and Li/Na metal can be distinguished according to the atomic number Z-contrast. The bright and dark spots indicate TMs and Li/Na atoms, respectively. Figure 1c shows the aberration corrected HAADF-STEM image of the pristine material. There is no heteroatom in the TMs layers due to the same arrangement and brightness according to the 2D plan map and 3D surface plot (the inset of top-right). The same intensity of line profile illustrates there are no impurity atoms in the Li layers. As a comparison, Figure 1d represents the 2D plan map of the NSO sample. The brightest dots are derived from the heavy TM atoms (Ni and Mn) because the brightness is proportional to the atomic number ($Z^{1.7}$). Other sites imply Li atoms in the TMs layers or Li/Na atoms in the Li layers. It should be noted that the area shown in the square box, especially the positions indicated by arrows, means Si element doping. This result also indicates the doping depth is approximately 5 nm from the interface of bulk and coating layer, and it is consistent with the previous reports about coating induced doping.[31-33] In order to vividly display the Si doping, the block 2D image region is converted to the 3D surface plot as Figure 1e iii shows, the light blue arrows mean Si doping and the white circles indicate Li atoms. The line profiles (i and ii) in Figure 1e stem from the red rectangle region i and the yellow rectangle region ii in Figure 1d, respectively. The yellow rectangle (ii) area indicates there is no impurity atom in the Li layer, which can be confirmed by the same intensity of line profile (ii) in Figure 1e. However, compared to the region (ii), the area (i) shows Na ions doping in the Li layer, which can be further

confirmed by the line profile (i) in Figure 1e. Because Na atomic number is higher than that of Li atoms it can exhibit higher intensity or peaks (above the red line) in the sodium atoms doped Li layer as shown by the line profile (i) in Figure 1e.

Figure 2 shows the electrochemical performances of three samples. The initial discharge capacity of pristine, Li_2SiO_3 (LSO) and Na_2SiO_3 (NSO) samples is 246, 247 and 254 mAh g^{-1} at current density of 0.05 C (1C = 250 mA / g), respectively (Figure 2a). However, the Coulombic efficiency of pristine sample is lowest in the three samples, which can be ascribed to the longest charge plateau at ~4.5 V. This profile is caused by the lattice oxygen loss in the form of O_2.[17] In contrast, the coating samples perform excellent structural stability, especially for the NSO sample, which denotes the lattice oxygen can be stabilized by the synergic effect of coating and co-doping. The rate performance is shown in Figure 2b. All batteries are activated at 0.05 C, then the charge-discharge cycles are conducted from 0.1 C to 10 C, and finally go back to 0.1 C. The discharge capacity of all samples decreases with the increasing current density, but the performance of the coated samples is better than that of the pristine material, which can be ascribed to the advantages of the coating layer and surface doping.[34, 35] However, what interests us is the difference between LSO coating and NSO coating. The discharge capacity of LSO and NSO coated samples is similar at low current density. As a comparison, the performance of NSO sample is much better than that of LSO coating material when the current density is over 2C. Especially, the discharge capacity of NSO is approximately 110 mAh g^{-1} at 10 C, which is higher than that of LSO (~85 mAh g^{-1}). All of these results can be explained by the synergy effect of NSO coating

and Na^+/Si^{4+} co-doping. At a low current density, the Li^+ can be fully inserted and extracted due to the sufficient reaction time in both samples. However, at a high current density, the electrochemical reaction entered to the discharge process before Li^+ is fully extracted during charging process for the LSO with narrower Li^+ diffusion channel, while more Li^+ is extracted in the NSO sample due to the wider Li^+ diffusion channel. In summary, first, the Li^+ diffusion can be improved by the <mark>Na^+-conductive</mark> coating layer. Then, the Na^+ is doped into the Li^+ layers, causing a pinning effect and expanding the Li ion diffusion channel due to the larger ion radius.[8] The crystal structure is stabilized due to Si doping into the TM layers because Si-O binding energy (798 KJ mol^{-1}) is higher than that of Mn-O bonding energy (402 KJ mol^{-1}) and Ni-O bonding energy (391.6 KJ mol^{-1}). The discharge capacity of NSO can return to about 236 mAh g^{-1}. As a comparison, the discharge capacity of LSO sample cannot reach the original state, which means the Na^+ and Si^{4+} co-doping can enhance the electrochemical reversibility. Figure 2c shows the long cycles performance of the three samples at 5 C. The discharge curve of the NSO sample is smooth and the capacity shows almost no attenuation compared with those of LSO and pristine material. The Figure 2d presents the voltage fading during the charge-discharge cycles. We can clearly find the voltage fading is notably suppressed from 3.54 V to 3.28 V after 500 cycles at 5 C for the NSO sample (0.52 mV/cycle). In contrast, the voltage fading for pristine sample is more remarkable from 3.44 V to 3.02 V at a rate of 0.84 mV/cycle and the voltage decay for LSO sample is also still very serious (3.47 V to 3.10 V, 0.74 mV/cycle). The comparison of voltage attenuation has been carried out in the Table S2, and the NSO sample has the

minimal voltage fading in these studies. These excellent electrochemical properties can be attributed to "Three-in-One" effect. Na_2SiO_3 coating can suppress the oxygen release and the accompanying Na/Si co-doping further stabilizes the lattice structure and improve the kinetics of Li^+. The detailed investigation can be described in the following.

To verify the influence of NSO coating and the surface co-doping on the Li^+ diffusion kinetics, the characterization methods of PITT and EIS have been applied, as shown in Figure S3 and S4. The Li ion diffusion coefficient (D_{Li}) can be calculated by the following formula: [36, 37]

$$D_{Li} = - [\mathrm{dln}(I) \, / \, dt] \cdot [4L^2 / \, \pi^2]$$

I, t and L represent the current, time and Li^+ diffusion thickness, respectively. The D_{Li} value of NSO sample is obviously better than those of pristine and LSO samples during the charging and discharging process, which can be ascribed to the increased energy barrier for Ni^{2+} migrating to the octahedral vacancies in Li^+ layers due to Na^+ doping in the Li ion layers, and meanwhile, the larger radius Na^+ instituted in Li^+ layers can expand the Li ion transfer channels.[38] Moreover, the increased D_{Li} can be attributed to the Si^{4+} doping into the TM layers and the NSO coating, which can reduce the oxygen evolution due to the higher Si-O bonding and suppress the oxygen release due to the coating layer. Similar to the first charging, Li^+ inserts more easily to the octahedral vacancies in Li ion layers during the discharge process due to the expanded I_{LiO2} caused by the Na^+. This insertion enhances the Li^+ diffusion as shown in Figure S3. The EIS also is used to characterize the interfacial resistance. Figure S4a and b show the EIS patterns of three samples before cycling and after 500 cycles at 5C, respectively. The

semicircle usually expresses the interfacial resistance for Li$^+$ migration between electrolyte and cathode particles. As shown in Figure S4, the impedance of NSO is minimal before and after cycling, which can be explained by the coating and co-doping to improve the Li$^+$ diffusion kinetics.

In addition, the excellent kinetics and related electrochemical performances can also be illustrated by the dQ/dV curves, as shown in Figure S5. The peaks at ~4.4 V and at ~3.25 V are indexed to the redox couples of Ni^{4+}/Ni^{2+} and Mn^{4+}/Mn^{3+} as shown in the purple and green areas, respectively. The shift of both peaks of pristine sample is more drastic than that of the NSO sample in the first 55 cycles meaning the structure of the NSO sample is more stable than that of pristine material, which can explain the outstanding cyclic stability. Especially, the peaks of pristine shift more obvious in green shadows because of the severe sluggish kinetics and voltage hysteresis, which also can be attributed to the transformation from layered structure to spinel structure, which is the devil for voltage fading. Therefore, the NSO coating and co-doping synergy effect can enhance the kinetics, suppress the phase transformation and the voltage decay. The outstanding cycling stability is also reflected by the DSC. Figure S6 shows the DSC pattern of three samples upon charging to 4.8 V and keeping for 30 min. The exothermic peaks of the NSO sample are 299.0°C and the heat generation is 332.2 J/g. In comparison, the corresponding values of pristine material are 284.0°C and 451.6 J/g, respectively. This result shows the NSO coating sample has better thermal stability, which can be attributed to the coating layer of Na$_2$SiO$_3$ and higher Si-O binding which stabilizes lattice oxygen due to the Si doping.

The diffraction peaks obtained by *in situ* XRD of both pristine and NSO samples at first cycle are shown in Figure 3, and the main peaks (003), (101) and (104) are indexed to the layered structure and the peaks of Be/BeO at approximately 18.1° and 44.05° marked with an asterisk. First, during the charging process, the (003) peak moves to lower 2θ angle while the (101) and (104) peaks shift towards high 2θ angle, which can be ascribed to the increased lattice unit c and decreased a parameter, respectively.[39] The increased c is caused by Li^+ deintercalation from the Li ion layers, which can improve the electrostatic repulsion between adjacent oxygen layers and the dropped value a is due to the oxidation of Ni^{2+} to Ni^{3+}/Ni^{4+}, which creates smaller ionic radius.[38,40] Then, in the discharge section, there is an inverse change for the three peaks. The contraction of Li^+ layers and the decrease of c parameter can be attributed to the reduced electrostatic repulsion between oxygen layers caused by Li insertion into the Li^+ layers. The increase in *a* parameter can be ascribed to the reduction of TM^{4+} that increase the TM radius. It is worth noting that the magnitude of shift of the pristine sample is larger than that of NSO as shown in Figure 3a and b, respectively, and these results are in agreement with the change of *ex situ* XRD results shown in Figure S7. According to the above analysis, the Na^+ doping into the Li^+ layers as a pillar can play a pinning effect, which can avoid the dramatic change in electrostatic repulsion between oxygen layers when Li^+ ions extract from Li ion layers, which can stabilize the lattice oxygen and enhance the anion oxygen redox. Moreover, the Si doping is favorable to the stability of TM layers which can also avoid dramatic structural changes and the collapse of the layer structure. Therefore, the stable structure enhances the excellent electrochemical

cyclic performances.

To elucidate the change of electronic structure and the variation of the local structure during the initial cycle, X-ray absorption near-edge structure (XANES) measurements have been used as shown in Figure 4. First, we characterize the *ex situ* XANES of pristine and NSO samples at different voltage stages in Figure 4a-d. In general, the oxide states of transition metals are closely related to the absorbing edge, and the shape of peaks is sensitive to the local coordination structure of transition metals.[41] The Mn K-edge XANES spectra of pristine and NSO samples are shown in Figure 4a and c, respectively. It confirms the average valence of Mn in both the samples is +4 compared with the metal oxide references (MnO, Mn_2O_3 and MnO_2). Figure 4a and c shows no discernible change in the absorbing edges except for a slight vibration in the peak shapes, which means the average valence of Mn is stable but the coordination environment slightly changes during the charge-discharging process. In addition, the coordination information can be further displayed by the pre-peaks as shown by the insets and by the white line as the highest peaks. The intensity and position of the pre-peak are closely related to the MnO_6 octahedral coordination, and the shape of the white line is identified by the charge state of materials and occupancy of the p-states.[42] According to the white lines shown in Figure 4a and c, the changes in the pristine material are more pronounced than those of NSO. Especially, compared with the NSO, the white line of pristine material cannot return to the initial state when discharged to 2.0 V indicating the coated and doped sample undergoes a reversible coordination change, which can also be verified by the rate performance in Figure 2b.

The capacity of NSO can return to the initial value when back from 10 C to 0.1 C. Figure 4b and d show the Ni K-edge spectra of both samples, comparing the reference (NiO) with both samples at open-circuit voltage (OCV) state, it shows the value of Ni is +2. The Ni K-edges shift continuously to higher energy during charging. When both cathode materials are charged to 4.65V, the absorbing edges of the nickel shift to the highest energy region, indicating the Ni^{2+} are oxidized to Ni^{4+}. It is worth noting that the energy of nickel K-edge shifts back to the lower energy region when charged to 4.8 V, and this change of pristine material is more dramatic than that of NSO, indicating part of the nickel ions migrate to the Li ion layers.[43, 44] When discharging to 2.0 V, the spectra of Ni K-edge shift towards the initial state. Whereas, that of NSO can completely return to the OCV state compared with the spectrum of pristine material. This reveals that charge compensation of cations mainly comes from the nickel redox, the cation mixing can be suppressed, and the reversibility and cyclic stability can be improved by the coating and co-doping synergy effect.

In addition, the stability of structure can be confirmed by the XANES results for different cycles as shown in Figure 4e-h. The XANES spectra of pristine and NSO samples at the Mn and Ni K-edge with the first 50th cycles are given in Figure 4e, f and Figure 4g, h, respectively. Figure 4e and g show the spectra of Mn K-edge with different cycles. The energy of Mn K-edge of both samples shifts to lower energy with the increase of cycle numbers, indicating the reduction of Mn oxidation state with increasing cycling number. However, the spectra of pristine material shift continuously to lower energy with the cycles from OCV state to the 50th cycle. For comparison, the

17

XANES spectra of the NSO sample remain unchanged from the 10th to the 50th cycle, meaning the stability of structure can be enhanced by coating and co-doping synergy effects. This point can be further illustrated by the XANES spectra of Ni K-edge shown in Figure 4f and h. The position and intensity of Ni K-edge have hardly changed in the NSO sample compared with those of the pristine sample, indicating the nickel ions are stable and they cannot easily migrate from the TM layers to Li ions layers since the Si^{4+} doping and the coating layer prevents erosion by electrolyte.

The excellent electrochemical performances and stable structure can also be illustrated by the operando differential electrochemical mass spectrometry (DEMS). Figure 5 shows the oxygen production of the pristine and NSO samples. One significant difference is that the O_2 production of the uncoated sample is much more (0.28 μmol mg^{-1}) than that of the NSO sample (0.13 μmol mg^{-1}). The reduced oxygen amount of the NSO sample can be ascribed to the synergetic effect of coating and Si/Na co-doping. Therefore, there are fewer side reactions between electrolyte and oxygen, which can reduce the corrosion of layer structure, together with the coating layer and co-doping, all of these reduce the dissolution of TMs and enhance the stability of layer structure as shown in Figure 4. It is consistent with the excellent electrochemical performances of the NSO sample.

To further study the anionic redox chemistry process, O K-edge RIXS spectra under different charge-discharge states were obtained at U41-PEAXIS beamline of HZB.[45, 46] It can clarify the chemical state of oxygen due to the emission photons accompanying the transition of electrons from the valence band to core hole states.

Figure 6a and b represent the RIXS of O K-edge of pristine and NSO samples, respectively, which are collected at an incident energy of 531 eV. There is a striking new peak at emission energy of 523.6 eV for both samples when charge to 4.8 V, and disappears when discharged to 2.0 V. This peak is similar to the previous reports and is classified as the fingerprint of oxygen redox chemistry.[47-49] In addition, the growing intensity of elastic peak at 531 eV for samples charged to 4.8 V illustrates that more oxygen holes are created. In comparison, the elastic peak intensity of the NSO sample is stronger than that of pristine material indicating better oxygen redox activity of the NSO sample. What attracts us are the inelastic peaks near the elastic line as shown in the insets, which can be ascribed to the oxygen molecule and the MnO_6 octahedral coordination,[37, 49-51] but further research is needed. These peaks of the NSO sample are more regular compared to the pristine sample. We believe that this is caused by the distortion of MnO_6 octahedron rather than an array of cations rearrangement due to the stable structure caused by the Na/Si doping. Moreover, the XPS analysis has been performed for both samples charged to 4.8 V with different detection thicknesses. The O 1s spectra are shown in Figure 6c and d. First, four peaks can be observed at approximately 529.5 eV (green area), 530.5 eV (purple area), 531.5 eV (yellow area) and 533.0 eV (light blue area) before sputtering with argon ions, which can be ascribed to the crystalline network (O^{2-}), lattice oxygen (O^- / O_2^{2-}), surface absorbed species and electrolyte oxidation, respectively. These results agree with the work of Tarascon et al.[52] The peak attributed to electrolyte oxidation almost disappears at ~533.0 eV after thinning the specimens to 50 nm and 100 nm in both samples as Figure 6c and d shown.

For comparison, the purple peak assigned to O⁻ or/and O_2^{2-} in the NSO sample is bigger than that of pristine material before etching and after etching. The larger proportion of purple area means there is more oxygen anion participating in the anionic redox for the charge compensation both in the surface and bulk of samples. Therefore, the higher capacity can be attributed to the enhanced anionic redox chemistry in the NSO sample.

The above results have directly proved the structural stability and enhanced anionic redox chemistry. To further rationalize the results, DFT calculations have been conducted. At first, the optimized models of crystal structure are created as shown in Figure S8. The yellow and blue spheres represent the Na atom in the Li⁺ layer and Si atom in the transition metal layer, respectively. Based on this model, the density of state (DOS) and electron location function (ELF) are calculated (Figure 7). Figure 7a shows the DOS patterns of both samples, we can find the pseudo gap is narrower in the NSO sample due to the proximity of two peaks near the Fermi level as the arrows shown, which indicates a slight decrease of covalency in the NSO sample, and this is in favor of suppressing the change of O 2p band and enhancing the reversibility of anionic redox chemistry during the charge and discharge process. Therefore, the oxygen release is reduced and the cyclic stability is enhanced. Figure 7b, c and d, e show the ELF patterns of the pristine sample and the NSO material, respectively. It is found the difference of the electron density distribution is small along (504) plane with Na atoms, meaning the effect of sodium atoms is limited for the electron density in the Li ion layers due to the similar electronic structure between Na atom and Li atom (Figure 7b and d). As a

comparison, there are more delocalized electron (green area) in the (001) plane, and this plane goes through Si atoms in the NSO sample in Figure 7e. This result means the NSO sample has higher conductivity. Moreover, the delocalized electrons may be conducive to the cationic redox. This calculated result is consistent with the XAS.

To further understand the kinetic effect for the excellent performances, the migration energy barrier of the Li ions diffusion is calculated using the ==NEB== method. The calculation parameters and convergence criteria are kept the same as in the ground state calculations. Figure 7f and g show the Li^+ diffusion paths of the pristine and the NSO sample, respectively. We can visually see that it is easier for the Li ions migration between two adjacent neighboring octahedral by passing through the intermediate tetrahedral position in the NSO sample. Moreover, Figure 7h shows the quantitative migration barrier of both samples. It shows the migration energy barrier of the NSO sample just is 0.096 eV, which is 0.063 eV lower than that of the pristine sample (0.159 eV), and this is consistent with the results of diffraction and PITT.

4. Conclusion

In conclusion, Na_2SiO_3 has been successfully coated on the surface of LMNO cathode material by a facile method, which brings a "three-in-one" effect on the improvement of the structure and electrochemical performance: Na_2SiO_3 coating, Na doping and Si doping. The Na^+ diffuses into the Li layers and Si^{4+} diffuses into the TM layers from the coating layer during the calcination process. The increased Li ion diffusion layers are beneficial to the kinetics of Li^+ mitigation, the contracted TMs layers and the strong Si-O bonding are favorable to the stability of the layered structure.

All of these enhance the rate capability and stability of cycles. Especially, the slightly decreased covalency of TM-O bonding suppresses the oxygen evolution and enhances the reversibility of anion redox chemistry. Moreover, the coating layer Na_2SiO_3 can also reduce the oxygen release and protect the bulk phase from the dissolution and migration of TMs, which has been confirmed by the *ex situ* XAS. This synergetic strategy of one stone and three birds can also be extended to modify other cathode materials.

Supporting Information

Supporting Information is available online at http://pubs.acs.org. It includes the results of XRD refinement, TEM, SEM, PITT, EIS, dQ/dV, DSC, ex-situ XRD and calculation model. The information table of joint Rietveld Refinement and the comparison table of voltage fading.

References

1.   Lee, J.; Kitchaev, D. A.; Kwon, D.-H.; Lee, C.-W.; Papp, J. K.; Liu, Y.-S.; Lun, Z.; Clément, R. J.; Shi, T.; McCloskey, B. D.; Guo, J.; Balasubramanian, M.; Ceder, G., Reversible Mn2+/Mn4+ double redox in lithium-excess cathode materials. *Nature* **2018,** 556, (7700), 185-190.

2.   Li, M.; Lu, J.; Chen, Z.; Amine, K., 30 Years of Lithium-Ion Batteries. *Adv. Mater.* **2018,** 30, (33), 1800561.

3.   Goodenough, J. B.; Park, K. S., The Li-ion rechargeable battery: a perspective. *J. Am. Chem. Soc.* **2013,** 135, (4), 1167-76.

4.   Assat, G.; Tarascon, J.-M., Fundamental understanding and practical challenges of anionic redox activity in Li-ion batteries. *Nat. Energy* **2018,** 3, (5), 373-386.

5.   Schmuch, R.; Wagner, R.; Horpel, G.; Placke, T.; Winter, M., Performance and cost of materials for lithium-based rechargeable automotive batteries. *Nat. Energy* **2018,** 3, (4), 267-278.

6.   Liu, P.; Zhang, H.; He, W.; Xiong, T.; Cheng, Y.; Xie, Q.; Ma, Y.; Zheng, H.; Wang, L.; Zhu, Z. Z.; Peng, Y.; Mai, L.; Peng, D. L., Lithium Deficiencies Engineering in Li-Rich Layered Oxide Li1.098Mn0.533Ni0.113Co0.138O2 for High-Stability Cathode. *J. Am. Chem. Soc.* **2019,** 141, (27), 10876-10882.

7.   House, R. A.; Maitra, U.; Perez-Osorio, M. A.; Lozano, J. G.; Jin, L.; Somerville, J. W.; Duda, L. C.; Nag, A.; Walters, A.; Zhou, K. J.; Roberts, M. R.; Bruce, P. G., Superstructure control of first-cycle voltage hysteresis in oxygen-redox cathodes. *Nature* **2020,** 577, (7791), 502-508.

8.   Qing, R.-P.; Shi, J.-L.; Xiao, D.-D.; Zhang, X.-D.; Yin, Y.-X.; Zhai, Y.-B.; Gu, L.; Guo, Y.-G., Enhancing the Kinetics of Li-Rich Cathode Materials through the Pinning Effects of Gradient Surface Na+ Doping. *Adv. Energy Mater.* **2016,** 6, (6), 1501914.

9.   Ates, M. N.; Jia, Q.; Shah, A.; Busnaina, A.; Mukerjee, S.; Abraham, K. M., Mitigation of Layered to Spinel Conversion of a Li-Rich Layered Metal Oxide Cathode Material for Li-Ion Batteries. *J. Electrochem. Soc.* **2014,** 161, (3), A290-A301.

10.   Wynn, T. A.; Fang, C.; Zhang, M.; Liu, H.; Davies, D. M.; Wang, X.; Lau, D.; Lee, J. Z.; Huang, B.-Y.; Fung, K.-Z.; Ni, C.-T.; Meng, Y. S., Mitigating oxygen release in anionic-redox-active cathode materials by cationic substitution through rational design. *J. Mater. Chem. A* **2018,** 6, (47), 24651-24659.

11.   Ma, J.; Yan, H.; Li, B.; Xia, Z.; Huang, W.; An, L.; Xia, D., Tuning the Electronic Structure of the Metal–Oxygen Group by Silicon Substitution in Lithium-Rich Manganese-Based Oxides for Superior Performance. *J. Phys. Chem. C* **2016,** 120, (25), 13421-13426.

12.   An, J.; Shi, L. Y.; Chen, G. R.; Li, M. S.; Liu, H. J.; Yuan, S.; Chen, S. M.; Zhang, D. S., Insights into the stable layered structure of a Li-rich cathode material for lithium-ion batteries. *J. Mater. Chem. A* **2017,** 5, (37), 19738-19744.

13.   Chen, G.; An, J.; Meng, Y.; Yuan, C.; Matthews, B.; Dou, F.; Shi, L.; Zhou, Y.; Song, P.; Wu, G.; Zhang, D., Cation and anion Co-doping synergy to improve structural stability of Li- and Mn-rich layered cathode materials for lithium-ion batteries. *Nano Energy* **2019,** 57, 157-165.

14.   Liu, S.; Liu, Z.; Shen, X.; Li, W.; Gao, Y.; Banis, M. N.; Li, M.; Chen, K.; Zhu, L.; Yu, R.; Wang, Z.; Sun, X.; Lu, G.; Kong, Q.; Bai, X.; Chen, L., Surface Doping to Enhance Structural Integrity and Performance of Li-Rich Layered Oxide. *Adv. Energy Mater.* **2018,** 8, (31), 1802105.

15.   Shin, Y.; Kan, W. H.; Aykol, M.; Papp, J. K.; McCloskey, B. D.; Chen, G.; Persson, K. A., Alleviating oxygen evolution from Li-excess oxide materials through theory-guided surface protection. *Nat.*

Commun. **2018,** 9, (1), 4597.

16.   Yang, H.; Wu, H. H.; Ge, M.; Li, L.; Yuan, Y.; Yao, Q.; Chen, J.; Xia, L.; Zheng, J.; Chen, Z.; Duan, J.; Kisslinger, K.; Zeng, X. C.; Lee, W. K.; Zhang, Q.; Lu, J., Simultaneously Dual Modification of Ni-Rich Layered Oxide Cathode for High-Energy Lithium-Ion Batteries. *Adv. Funct. Mater.* **2019,** 29, (13), 1808825.

17.   Zhang, X. D.; Shi, J. L.; Liang, J. Y.; Yin, Y. X.; Zhang, J. N.; Yu, X. Q.; Guo, Y. G., Suppressing Surface Lattice Oxygen Release of Li-Rich Cathode Materials via Heterostructured Spinel Li4Mn5O12 Coating. *Adv. Mater.* **2018,** 30, 1801751.

18.   Li, Q.; Zhou, D.; Zhang, L.; Ning, D.; Chen, Z.; Xu, Z.; Gao, R.; Liu, X.; Xie, D.; Schumacher, G.; Liu, X., Tuning Anionic Redox Activity and Reversibility for a High-Capacity Li-Rich Mn-Based Oxide Cathode via an Integrated Strategy. *Adv. Funct. Mater.* **2019,** 29, (10), 1806706.

19.   An, K.; Skorpenske, H. D.; Stoica, A. D.; Ma, D.; Wang, X.-L.; Cakmak, E., First In Situ Lattice Strains Measurements Under Load at VULCAN. *Metall. Mater. Trans. A* **2011,** 42, (1), 95-99.

20.   Calder, S.; An, K.; Boehler, R.; Dela Cruz, C. R.; Frontzek, M. D.; Guthrie, M.; Haberl, B.; Huq, A.; Kimber, S. A. J.; Liu, J.; Molaison, J. J.; Neuefeind, J.; Page, K.; dos Santos, A. M.; Taddei, K. M.; Tulk, C.; Tucker, M. G., A suite-level review of the neutron powder diffraction instruments at Oak Ridge National Laboratory. *Rev. Sci. Instrum.* **2018,** 89, (9), 092701.

21.   Larson, A. C.; Dreele, R. B. V., General Structure Analysis System (GSAS). Los Alamos National Laboratory Report LAUR 2004, 86-748.

22.   Kresse, G.; Furthmüller, J., Efficiency of ab-initio total energy calculations for metals and semiconductors using a plane-wave basis set. *Comput. Mater. Sci.* **1996,** 6, (1), 15-50.

23.   Blöchl, P. E., Projector augmented-wave method. *Phys. Rev. B* **1994,** 50, (24), 17953-17979.

24.   Perdew, J. P.; Burke, K.; Ernzerhof, M., Generalized Gradient Approximation Made Simple. *Phys. Rev. Lett.* **1996,** 77, (18), 3865-3868.

25.   Kresse, G.; Joubert, D., From ultrasoft pseudopotentials to the projector augmented-wave method. *Phys. Rev. B* **1999,** 59, (3), 1758-1775.

26.   Liang, G.; Wu, Z.; Didier, C.; Zhang, W.; Cuan, J.; Li, B.; Ko, K. Y.; Hung, P. Y.; Lu, C. Z.; Chen, Y.; Leniec, G.; Kaczmarek, S. M.; Johannessen, B.; Thomsen, L.; Peterson, V. K.; Pang, W. K.; Guo, Z., A Long Cycle-Life High-Voltage Spinel Lithium-Ion Battery Electrode Achieved by Site-Selective Doping. *Angew. Chem. Int. Ed.* **2020,** 59, (26), 10594-10602.

27.   Liu, Y.; Ning, D.; Zheng, L.; Zhang, Q.; Gu, L.; Gao, R.; Zhang, J.; Franz, A.; Schumacher, G.; Liu, X., Improving the electrochemical performances of Li-rich Li1.20Ni0.13Co0.13Mn0.54O2 through a cooperative doping of Na+ and PO43− with Na3PO4. *J. Power Sources* **2018,** 375, 1-10.

28.   Zhang, J.; Gao, R.; Sun, L.; Zhang, H.; Hu, Z.; Liu, X., Unraveling the multiple effects of Li2ZrO3 coating on the structural and electrochemical performances of LiCoO2 as high-voltage cathode materials. *Electrochim. Acta* **2016,** 209, 102-110.

29.   Li, B.; Yan, H.; Ma, J.; Yu, P.; Xia, D.; Huang, W.; Chu, W.; Wu, Z., Manipulating the Electronic Structure of Li-Rich Manganese-Based Oxide Using Polyanions: Towards Better Electrochemical Performance. *Adv. Funct. Mater.* **2014,** 24, (32), 5112-5118.

30.   Ben Yahia, M.; Vergnet, J.; Saubanere, M.; Doublet, M. L., Unified picture of anionic redox in Li/Na-ion batteries. *Nat. Mater.* **2019,** 18, (5), 496-502.

31.   Hu, S.; Li, Y.; Chen, Y.; Peng, J.; Zhou, T.; Pang, W. K.; Didier, C.; Peterson, V. K.; Wang, H.; Li, Q.; Guo, Z., Insight of a Phase Compatible Surface Coating for Long-Durable Li-Rich Layered Oxide Cathode. *Adv. Energy Mater.* **2019,** 9, (34), 1901795.

32. Piao, J. Y.; Sun, Y. G.; Duan, S. Y.; Cao, A. M.; Wang, X. L.; Xiao, R. J.; Yu, X. Q.; Gong, Y.; Gu, L.; Li, Y. T.; Liu, Z. J.; Peng, Z. Q.; Qiao, R. M.; Yang, W. L.; Yang, X. Q.; Goodenough, J. B.; Wan, L. J., Stabilizing Cathode Materials of Lithium-Ion Batteries by Controlling Interstitial Sites on the Surface. *Chem* **2018,** 4, (7), 1685-1695.

33. Xiao, B.; Liu, H.; Liu, J.; Sun, Q.; Wang, B.; Kaliyappan, K.; Zhao, Y.; Banis, M. N.; Liu, Y.; Li, R.; Sham, T. K.; Botton, G. A.; Cai, M.; Sun, X., Nanoscale Manipulation of Spinel Lithium Nickel Manganese Oxide Surface by Multisite Ti Occupation as High-Performance Cathode. *Adv. Mater.* **2017,** 29, (47), 1703764.

34. Weigel, T.; Schipper, F.; Erickson, E. M.; Susai, F. A.; Markovsky, B.; Aurbach, D., Structural and Electrochemical Aspects of LiNi0.8Co0.1Mn0.1O2 Cathode Materials Doped by Various Cations. *ACS Energy Lett.* **2019,** 4, (2), 508-516.

35. Tang, M.; Yang, J.; Chen, N.; Zhu, S.; Wang, X.; Wang, T.; Zhang, C.; Xia, Y., Overall structural modification of a layered Ni-rich cathode for enhanced cycling stability and rate capability at high voltage. *J. Mater. Chem. A* **2019,** 7, (11), 6080-6089.

36. Kong, W.; Gao, R.; Li, Q.; Yang, W.; Yang, J.; Sun, L.; Liu, X., Simultaneously tuning cationic and anionic redox in a P2-Na0.67Mn0.75Ni0.25O2 cathode material through synergic Cu/Mg co-doping. *J. Mater. Chem. A* **2019,** 7, (15), 9099-9109.

37. Li, Q.; Ning, D.; Zhou, D.; An, K.; Wong, D.; Zhang, L.; Chen, Z.; Schuck, G.; Schulz, C.; Xu, Z.; Schumacher, G.; Liu, X., The effect of oxygen vacancy and spinel phase integration on both anionic and cationic redox in Li-rich cathode materials. *J. Mater. Chem. A* **2020,** 8, (16), 7733-7745.

38. Shen, C. H.; Huang, L.; Lin, Z.; Shen, S. Y.; Wang, Q.; Su, H.; Fu, F.; Zheng, X. M., Kinetics and structural changes of Li-rich layered oxide 0.5Li2MnO3.0.5LiNi0.292Co0.375Mn0.333O2 material investigated by a novel technique combining in situ XRD and a multipotential step. *ACS Appl. Mater. Interfaces* **2014,** 6, (15), 13271-9.

39. Lin, T.; Schulli, T. U.; Hu, Y.; Zhu, X.; Gu, Q.; Luo, B.; Cowie, B.; Wang, L., Faster Activation and Slower Capacity/Voltage Fading: A Bifunctional Urea Treatment on Lithium-Rich Cathode Materials. *Adv. Funct. Mater.* **2020,** 30, (13).

40. Ye, D.; Zeng, G.; Nogita, K.; Ozawa, K.; Hankel, M.; Searles, D. J.; Wang, L., Understanding the Origin of Li2MnO3 Activation in Li-Rich Cathode Materials for Lithium-Ion Batteries. *Adv. Funct. Mater.* **2015,** 25, (48), 7488-7496.

41. Gao, R.; Zhou, D.; Ning, D.; Zhang, W.; Huang, L.; Sun, F.; Schuck, G.; Schumacher, G.; Hu, Z.; Liu, X., Probing the Self-Boosting Catalysis of LiCoO2 in Li–O2 Battery with Multiple In Situ/Operando Techniques. *Adv. Funct. Mater.* **2020,** 30, (28), 2002223.

42. Erickson, E. M.; Sclar, H.; Schipper, F.; Liu, J.; Tian, R.; Ghanty, C.; Burstein, L.; Leifer, N.; Grinblat, J.; Talianker, M.; Shin, J.-Y.; Lampert, J. K.; Markovsky, B.; Frenkel, A. I.; Aurbach, D., High-Temperature Treatment of Li-Rich Cathode Materials with Ammonia: Improved Capacity and Mean Voltage Stability during Cycling. *Adv. Energy Mater.* **2017,** 7, (18), 1700708.

43. Koga, H.; Croguennec, L.; Ménétrier, M.; Mannessiez, P.; Weill, F.; Delmas, C.; Belin, S., Operando X-ray Absorption Study of the Redox Processes Involved upon Cycling of the Li-Rich Layered Oxide Li1.20Mn0.54Co0.13Ni0.13O2 in Li Ion Batteries. *J. Phys. Chem. C* **2014,** 118, (11), 5700-5709.

44. Yabuuchi, N.; Yoshii, K.; Myung, S.-T.; Nakai, I.; Komaba, S., Detailed Studies of a High-Capacity Electrode Material for Rechargeable Batteries, Li2MnO3-LiCo1/3Ni1/3Mn1/3O2. *J. Am. Chem. Soc.* **2011,** 133, (12), 4404-4419.

45. Lieutenant, K.; Hofmann, T.; Schulz, C.; Yablonskikh, M. V.; Habicht, K.; Aziz, E. F., Design concept of the high-resolution end-station PEAXIS at BESSY II: Wide-Q-range RIXS and XPS measurements on solids, solutions, and interfaces. *J. Electron Spectrosc. Relat. Phenom.* **2016,** 210, 54-65.

46. Schulz, C.; Lieutenant, K.; Xiao, J.; Hofmann, T.; Wong, D.; Habicht, K., Characterization of the soft X-ray spectrometer PEAXIS at BESSY II. *J. Synchrotron Radiat.* **2020,** 27, (1), 238-249.

47. Maitra, U.; House, R. A.; Somerville, J. W.; Tapia-Ruiz, N.; Lozano, J. G.; Guerrini, N.; Hao, R.; Luo, K.; Jin, L.; Perez-Osorio, M. A.; Massel, F.; Pickup, D. M.; Ramos, S.; Lu, X.; McNally, D. E.; Chadwick, A. V.; Giustino, F.; Schmitt, T.; Duda, L. C.; Roberts, M. R.; Bruce, P. G., Oxygen redox chemistry without excess alkali-metal ions in Na2/3[Mg0.28Mn0.72]O2. *Nat. Chem.* **2018,** 10, (3), 288-295.

48. Xu, J.; Sun, M.; Qiao, R.; Renfrew, S. E.; Ma, L.; Wu, T.; Hwang, S.; Nordlund, D.; Su, D.; Amine, K.; Lu, J.; McCloskey, B. D.; Yang, W.; Tong, W., Elucidating anionic oxygen activity in lithium-rich layered oxides. *Nat. Commun.* **2018,** 9, (1), 947.

49. Luo, K.; Roberts, M. R.; Hao, R.; Guerrini, N.; Pickup, D. M.; Liu, Y. S.; Edstrom, K.; Guo, J.; Chadwick, A. V.; Duda, L. C.; Bruce, P. G., Charge-compensation in 3d-transition-metal-oxide intercalation cathodes through the generation of localized electron holes on oxygen. *Nat. Chem.* **2016,** 8, (7), 684-91.

50. Luo, K.; Roberts, M. R.; Guerrini, N.; Tapia-Ruiz, N.; Hao, R.; Massel, F.; Pickup, D. M.; Ramos, S.; Liu, Y. S.; Guo, J.; Chadwick, A. V.; Duda, L. C.; Bruce, P. G., Anion Redox Chemistry in the Cobalt Free 3d Transition Metal Oxide Intercalation Electrode Li[Li0.2Ni0.2Mn0.6]O2. *J. Am. Chem. Soc.* **2016,** 138, (35), 11211-8.

51. House, R. A.; Rees, G. J.; Pérez-Osorio, M. A.; Marie, J.-J.; Boivin, E.; Robertson, A. W.; Nag, A.; Garcia-Fernandez, M.; Zhou, K.-J.; Bruce, P. G., First-cycle voltage hysteresis in Li-rich 3d cathodes associated with molecular O2 trapped in the bulk. *Nat. Energy* **2020**. https://doi.org/10.1038/s41560-020-00697-2.

52. Sathiya, M.; Rousse, G.; Ramesha, K.; Laisa, C. P.; Vezin, H.; Sougrati, M. T.; Doublet, M. L.; Foix, D.; Gonbeau, D.; Walker, W.; Prakash, A. S.; Ben Hassine, M.; Dupont, L.; Tarascon, J. M., Reversible anionic redox chemistry in high-capacity layered-oxide electrodes. *Nat. Mater.* **2013,** 12, (9), 827-35.
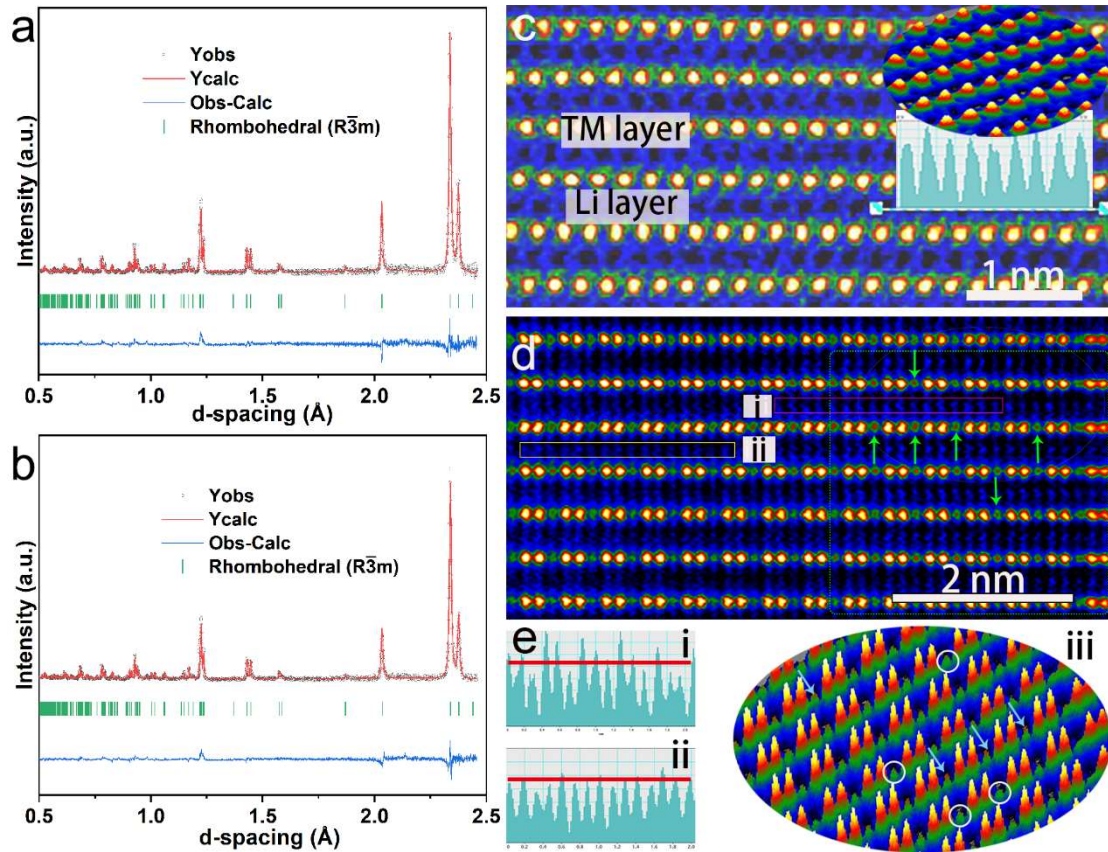
Figure 1. The NPD refinement results of (a) pristine and (b) NSO sample come from joint refinement. Aberration-corrected HAADF-STEM image of (c) pristine sample (the inset at top-right corner indicates the 3D atoms configuration and no impurity doping. The consistent intensity of line graph means only Li atoms in this layer) and (d) NSO sample. (e) The line profiles i and ii are from the rectangle boxes (i and ii) in (d) pattern. The 3D surface plot (iii) is derived from the green rectangle area in pattern (d). In the (d) and iii figures, the arrows represent the Si atoms doping.
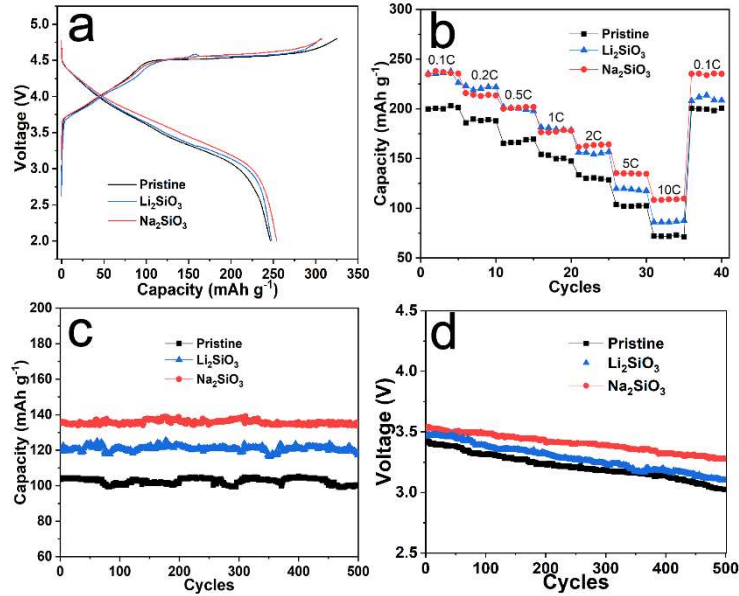
Figure 2. Electrochemical performances of pristine, LSO coated and NSO coated samples. (a) Initial charge-discharge curves at current density of 0.05 C, (b) Rate capacity, (c) the cyclic property, and (d) the pattern of voltage fading at current density of 5C.
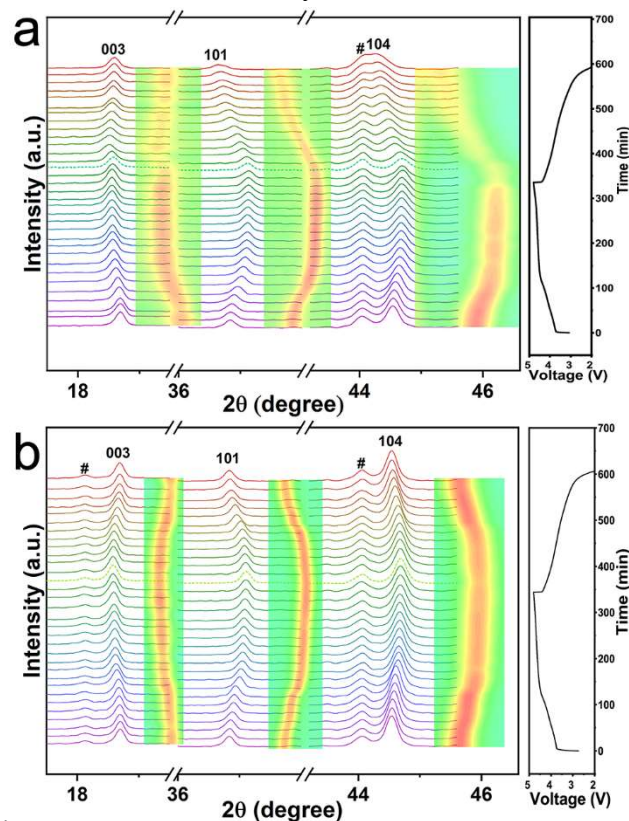

Figure 3. *In situ* XRD patterns tested during the first charge-discharge process of (a) pristine and (b) NSO samples. The hashtag represents Be/BeO, and the contour plots highlight the change of the left (003), (101) and (104) peaks in the both samples.
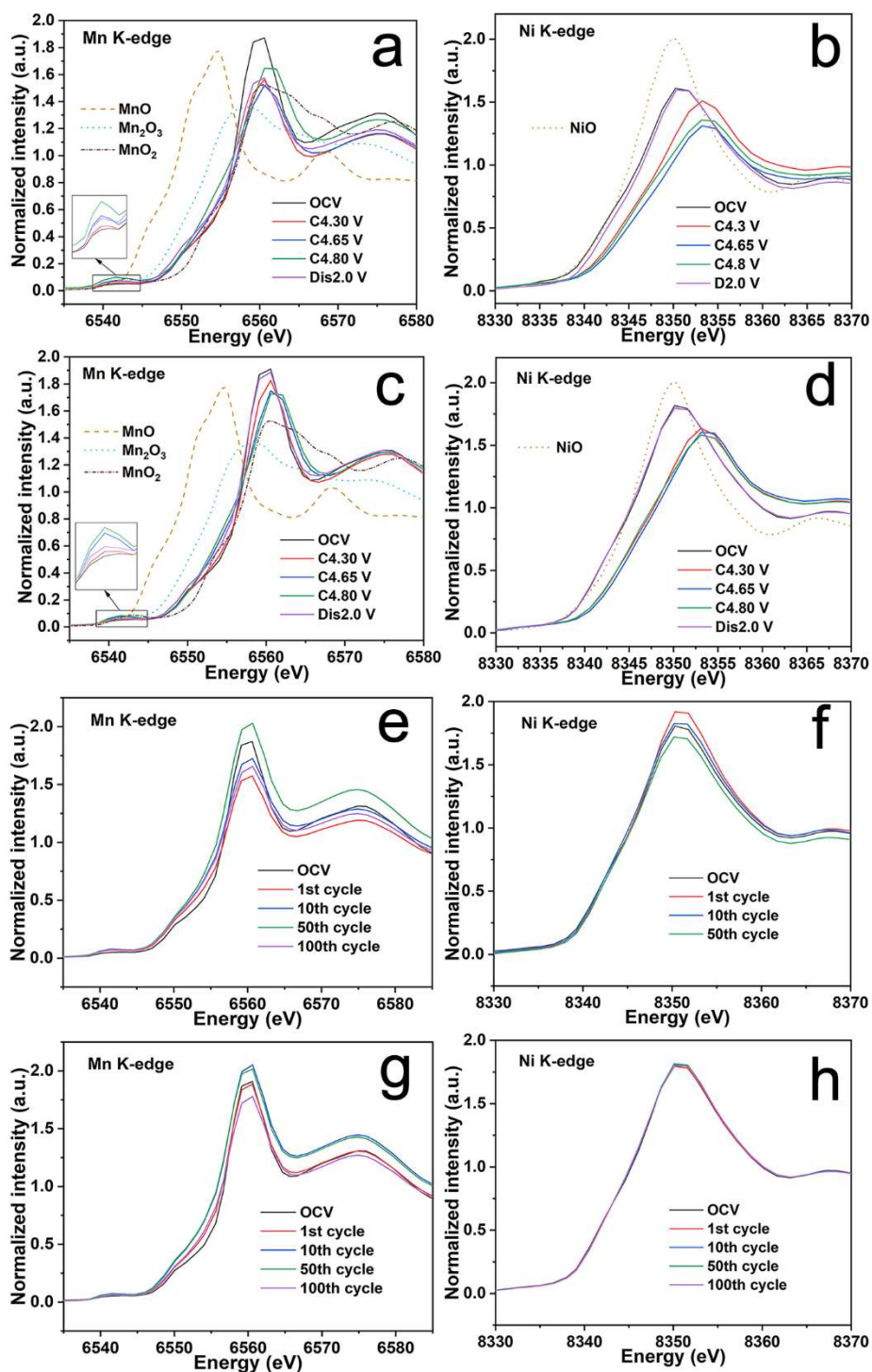
Figure 4 XANES spectra of Mn K-edge and Ni K-edge at different voltages and cycles. (a, b, e and f) for pristine and (c, d, g and h) for NSO samples.
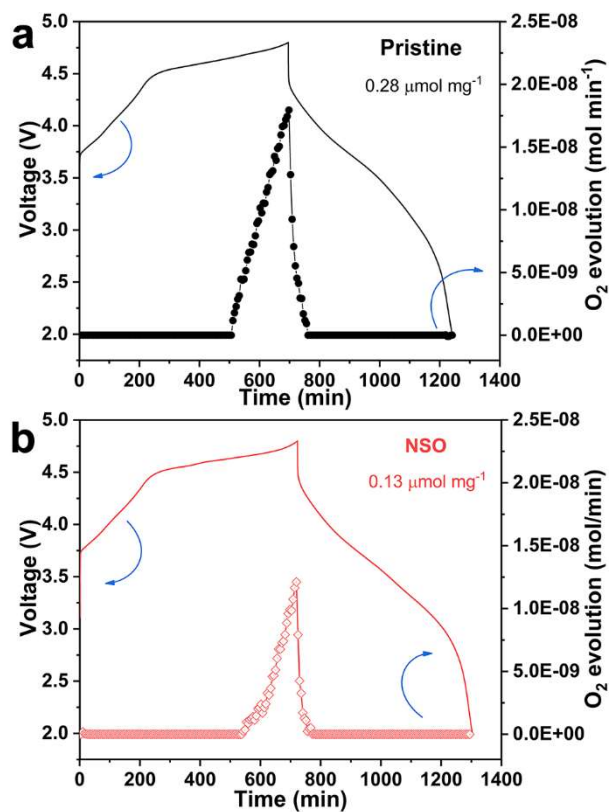
Figure 5. Operando differential electrochemical mass spectrometry of pristine and NSO sample, respectively. The current density is 0.1 C. The active material of pristine and NSO sample is 8 mg and 7.1 mg, respectively.
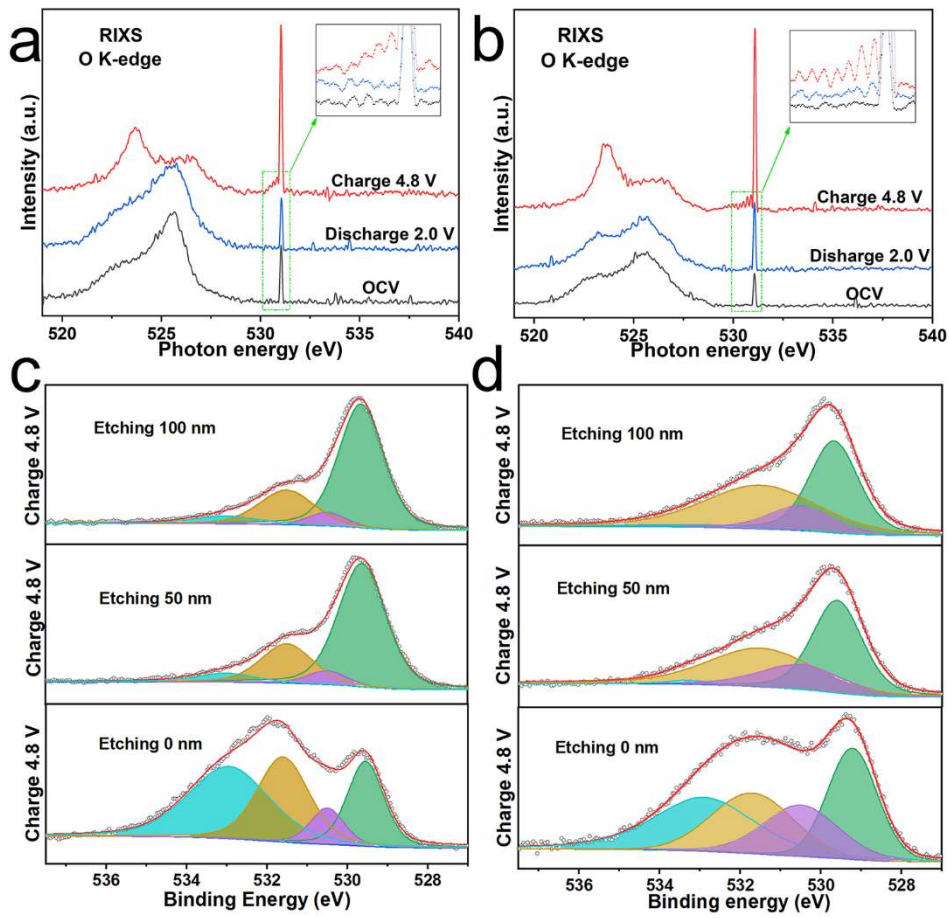
Figure 6. RIXS O K-edge of pristine material (a) and NSO sample (b), respectively, with an incident energy of 531 eV. XPS spectra of O 1s peaks for (c) pristine and (d) NSO samples at 4.8 V different Ar^+ etching thickness.
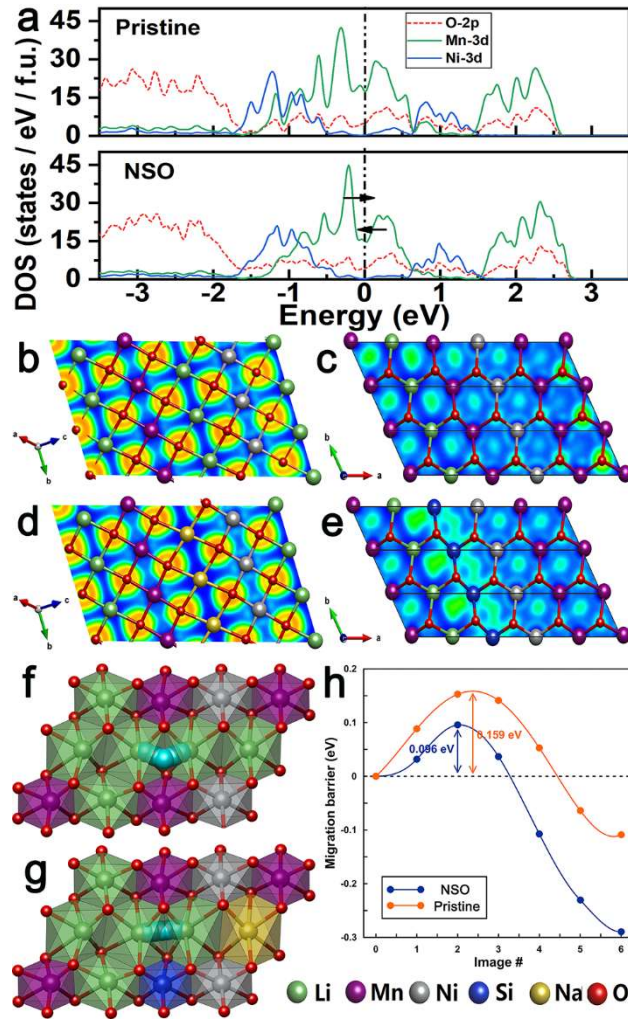
Figure 7. The density of state of (a) pristine and NSO samples. The electron localization function pattern of (b and c) pristine and (d and e) NSO samples, graphs (b and d) and (c and e) correspond to (504) and (001) planes, respectively. Illustration of Li$^+$ diffusion paths for (f) pristine and (g) NSO samples. (h) The calculated migration barrier of Li ions diffusion paths for both samples.

TOC

The anionic and cationic redox chemistry of $Li_{1.2}Mn_{0.6}Ni_{0.2}O_2$ have been enhanced via an integrated "Three-in-One" Strategy of Na_2SiO_3 coating, Na and Si co-doping. The synergetic strategy sheds some lights on exploring high-performance Li-rich cathode materials by tuning both anionic and cationic redox chemistry.